SiO$_2$-supported Fe & FeMn colloids—Fischer-Tropsch synthesis on 3D model catalysts

Feature Article

SiO₂-supported Fe & FeMn colloids—Fischer-Tropsch synthesis on 3D model catalysts

Mohammadhassan Dad [a], Remco J. Lancee [a], Matthys Janse van Vuuren [b], Jan van de Loosdrecht [b], J.W. Hans Niemantsverdriet [c], Hans O.A. Fredriksson [a,c,*]

[a] Laboratory for Physical Chemistry of Surfaces, Eindhoven University of Technology, P.O. Box 513, 5600 MB Eindhoven, The Netherlands
[b] Sasol, Group Technology, P.O. Box 1, Sasolburg 1947, South Africa
[c] SynCat@DIFFER, Syngaschem BV, P.O. Box 6336, 5600 HH Eindhoven, The Netherlands

ABSTRACT

A well-defined model catalyst constituting a compromise between high surface area, porous, industrial catalysts and a planar model catalyst has been developed. It allows for measurements of catalytic activity in micro reactors, where diffusion problems are kept at a minimum, while characterization both by surface science techniques and by bulk techniques can be applied. Monodisperse, non-porous SiO₂ microspheres with diameter 875 ± 25 nm have been synthesized, serving as the large area model support. These where then impregnated with pre-formed, monodisperse, colloidal Fe and FeMn nanoparticles resulting in a three-dimensional equivalent of a flat, Fe(-Mn)/SiO₂ model catalysts. Characterization with electron microscopy (SEM and TEM), X-ray photoelectron spectroscopy (XPS) and X-ray diffraction (XRD), before and after catalytic testing was performed. It was shown that the model catalysts can be used in Fischer-Tropsch synthesis experiments under industrially relevant conditions. The FTS experiments reveal that compared to the pure Fe catalyst, FeMn shows more stable activity, higher selectivity towards olefins and lower selectivity toward CH_4 and CO_2. Significant amounts of hydrocarbons on the catalyst surfaces and some minor indications of sintering were detected after the reaction. Formation of FeC_x was detected for the Fe catalyst while no significant amounts could be seen on the Mn-promoted catalyst.

1. Introduction

A typical heterogeneous catalyst consists of a variety of metal nanoparticles dispersed in the pores of a support particle. Some of the most relevant properties for a catalyst's activity are the geometry, morphology, structure and chemistry of the metal nanoparticles. Since these are concealed inside the support pores, it is therefore hard to perform an exhaustive characterization of such catalysts. Furthermore, diffusion of gaseous species in the pores can limit the catalytic reaction, making it complicated to recognize the origin of changes in the catalysts activity. A common method to overcome these difficulties is to study flat model catalysts or single crystals [1]. This allows for in depth characterization by different surface science techniques, under conditions ranging from ultra-high vacuum and liquid nitrogen temperature to more representative high pressure and temperatures. Model cat-

alyst studies have been performed to clarify the importance of a multitude of catalyst properties such as particle size and distribution, oxidation state, active sites, reactant and product binding energies and self-poisoning, alloying and faceting. However, flat model catalysts expose a very small active catalyst area. This makes them unsuitable for activity measurements, especially for catalysts and reactions with a low turnover frequency under realistic flow conditions. A non-porous powder model catalyst can play a role as a link between the high surface area, porous, industrial catalyst and the planar model catalyst [2,3].

Properly designed, such a model catalyst should be able to maintain the accessibility and high precision of a flat model catalyst while simultaneously allowing investigation of the catalytic activity under minimum gas diffusion limitations. In addition, the non-porous, powder model catalyst should allow for characterization studies where significant amounts of material are needed, like X-ray diffraction (XRD) or temperature programmed reduction or oxidation (TPR/TPO).

In this paper, we describe a model catalyst based on silica microspheres and monodisperse Fe nanoparticles, with and without Mn promoter. The Fe nanoparticles are anchored to the non-porous

silica spheres and the model catalysts were used in CO and H_2 oxidation experiments to demonstrate their performance in catalyst activity measurements (see Appendix A). The same catalysts were then used in a high pressure Fischer-Tropsch Synthesis (FTS) experiment. For background information on this important process we refer to recent overview articles [4,5]. The model catalysts were characterized by scanning and transmission electron microscopy (SEM and TEM), X-ray photoelectron spectroscopy (XPS) and XRD both during the synthesis process and after the catalytic testing.

2. Experimental

2.1. Characterization

SEM pictures were taken using a FEI Quanta 3D FEG dual beam, operated in high vacuum mode with an accelerating voltage of 2.5 kV. The samples were supported on carbon tape and the working distance was 9 mm.

TEM studies were carried out using a FEI Tecnai G^2 Sphera microscope operating with a 200 kV LaB$_6$ filament and a bottom mounted 1024 × 1024 Gatan CCD camera. All images were taken using the TEM in bright field mode. Samples were dispersed in ethanol and an appropriate amount of the sample was dropped onto a copper microscope grid covered with carbon windows.

XPS was measured with a K-Alpha AXIS Ultra spectrometer, equipped with a monochromated Al Kα X-ray source (1486.6 eV) and a delay-line detector (DLD). The spectra were obtained with the source operating at 150W and the background pressure in the analysis chamber during measurements was typically 1×10^{-8} mbar. Casa XPS software, Version 2.3.16 Pre-rel 1.4 was used for the data analysis. Binding energies were calibrated with the standard Si 2s = 154.6 eV peak in SiO_2.

The X-ray diffraction (XRD) patterns were recorded on a Bruker D$_2$ phaser using Cu Kα radiation (λ = 1.54 Å). Two theta angels from 10 to 70° were measured with a step size of 0.008° and a time per step of 0.5 s.

Attenuated total reflectance infrared spectroscopy (ATR-IR) spectra were recorded using a Nicolet Smart Golden Gate instrument equipped with a diamond crystal (cutoff at 800 cm^{-1}). Measurements were carried out using the appropriate background with a resolution of 2 cm^{-1} over 128 scans.

2.2. Model catalyst preparation

2.2.1. SiO$_2$ microspheres

SiO$_2$ microspheres (Stöber spheres) were synthesized according to the procedures described by Stöber et al. [6]. 71.5 ml of ethanol (Merck, absolute, for analysis) was added to 25 ml of ammonium hydroxide solution (28.0–30.0%, Merck, for analysis) followed by addition of 12 ml deionized water. The mixture was stirred for 3 min, before 6 ml of tetraethoxysilane (TEOS, Merck, for analysis) was added and the reaction allowed to run for another 3 h. The reaction mixture was then centrifuged for 12 min at 8000 rpm and the solid powder, consisting of silica micro spheres was separated from the solvent. The powder was subsequently dried overnight in an oven at 110 °C and then calcined at 400 °C (10 °C/min) for 4 h in an Ar gas flow containing 20 vol.% O_2.

2.2.2. Fe and Fe-Mn nanospheres

Colloidal Fe-nanoparticles were prepared with 0 and 10 mol% Mn as a promoter, according to [7–9]. Nanoparticles with these two compositions are henceforth referred to as Fe and Fe$_9$Mn$_1$. In short, first iron and manganese-oleates were prepared and mixed together in the desired molar rations. The solutions were then heated under nitrogen purging, to 320 °C, leading to thermal decompositions of the metal oleates, in turn leading to nucleation and growth of nanoparticles.

2.2.3. Fe & Fe-Mn on SiO$_2$ microspheres

The Fe and Fe$_9$Mn$_1$ nanoparticles were dissolved in toluene to obtain a solution with a 2 mmol metal concentration. The nanoparticle solutions were sonicated for 5 min and then mixed with calcined Stöber spheres to achieve a 5 wt.% Fe loading. These mixtures were further sonicated for 20 min and the toluene was evaporated slowly at 70 °C, yielding a black solid powder. This powder was dried overnight in an oven at 110 °C and subsequently calcined in 20% O_2/Ar at 350 °C (10 °C/min) for 6 h to obtain the powder Fe & FeMn/SiO$_2$ model catalysts. The size of the metal nanoparticles was estimated using the Image J software [10].

2.3. Fischer-Tropsch synthesis (FTS) experiments

FTS performance experiments were carried out in a stainless steel fixed-bed micro reactor tube (length 431 mm, inner diameter 7.92 mm) loaded with 500 mg of each catalyst sample (catalyst bed height 6 mm in the isothermal part of the reactor). The catalysts were reduced (activated) in-situ in pure CO at a flow of 500 ml/min and a gas hourly space velocity (GHSV) of 2300 h^{-1}. The samples were heated up from 25 °C to 270 °C at a rate of 5 °C/min and held at the targeted temperature for 24 h while the pressure was kept constant at 13 bar. The FTS products were analyzed with Agilant GC's. A detailed description is available in [11]

After reduction the reactor was flushed with Ar to evacuate the activation gas. In order to avoid catalyst damage due to high conversions and resulting high water partial pressures, a high GHSV = 10000 h^{-1} was first applied and then slowly decreased (during ~80 h) to the steady-state reaction conditions (270 °C, 13 bar, H_2/CO = 1). Hydrogen and carbon monoxide feed gas flow rates were controlled by two separate mass flow controllers (Brooks Delta II Smart Mass Flow SLA5850SICAB5C2A1) and the steady state experiments were conducted at GHSV = 2300 h^{-1} for 145 h. At the end of the experimental run the syngas was purged out with Ar and the reactor was allowed to cool down. At low temperature, the pressure was decreased and the reactor opened. For these experiments industrial grade H_2 from a pressure swing absorption (PSA) unit and CO from a hydroformylation unit was used. These gases were clean enough for normal Fischer Tropsch use and therefore no further cleaning was done. CO conversion and CO_2 selectivity was calculated per Eqs. (1) and (2):

$$CO\ conversion\,(\%) = 100 \times \frac{[CO]_{in} - [CO]_{out}}{[CO]_{in}} \tag{1}$$

$$CO_2\ selectivity\,(\%) = 100 \times \frac{[CO_2]_{out} - [CO_2]_{in}}{[CO]_{in} - [CO]_{out}} \tag{2}$$

where [CO] and [CO$_2$] are the molar concentrations of CO and CO_2 respectively.

The selectivity (%) toward the individual components relative to the CO converted to hydrocarbons (i.e. excluding CO converted to CO_2) was calculated per Eq. (3):

$$Hydrocarbon\ selectivity\,(\%) = 100 \times \frac{[j] \times j}{([CO]_{in} + [CO_2]_{in}) - ([CO]_{out} + [CO_2]_{out})} \tag{3}$$

where [j] is the molar concentration of a hydrocarbon chain with j carbon atoms. Olefin selectivity was calculated per Eq. (4):

$$Olefin\ selectivity\,(\%) = 100 \times \frac{[olefins]}{[olefins] + [paraffins]} \tag{4}$$

where [olefins] and [paraffins] are the molar concentrations of olefins and paraffins with all chain lengths summed.

All molar percentage data were then converted to selectivities on a weight basis.

3. Results

3.1. Model catalyst preparation

Fig. 1 shows electron microscopy pictures and XPS spectra of the Fe-Stöber model catalysts at different stages of the fabrication process.

Fig. 1(a) shows a SEM image of the calcined Stöber spheres (diameter of 875 ± 25 nm) prior to impregnation with metal nanoparticles. The corresponding XPS measurement (e) confirms that the calcined microspheres expose clean SiO_2 surfaces, with a minor peak deriving from adventitious carbon. Fig. 1 (b) shows the same spheres after impregnation with the iron nanoparticle solution and drying overnight at 110 °C. The oleic acid surfactant, used during the synthesis of the nanoparticles, is still present in between the Stöber spheres, resulting in coagulation of the spheres and that no iron nanoparticles can be distinguished. This is also clear from the XPS spectrum showing mainly a large carbon peak at 284.5 eV and only a minor Fe 2p peak around 710 eV stemming from the carbon-embedded iron particles. After calcination at 350 °C for 6 h, the oleic acid residues are removed and the metal nanoparticles can be observed on the spheres as brighter edges (Fig. 1(c)), which were not seen prior to impregnation. The removal of carbon precursors and presence of metal nanoparticles is also confirmed by the XPS measurements, now showing mainly peaks related to Fe, Si and O. No trace element contaminations are found in the XPS spectra. The detailed spectrum of the Fe 2p region (not shown) indicates that the iron nanoparticles are present as Fe^{3+}, as expected.

Fig. 1(d) shows a TEM image, zoomed in on one of the Stöber spheres, where it can clearly be seen how the Fe-nanoparticles are well dispersed and anchored to the surface. Although this is the case for most of the micro spheres, occasionally, the nanoparticles appear clustered together, forming domains with higher particle concentration on the Stöber spheres. These nanoparticle clusters are likely the bright spots which could be observed in Fig. 1(c).

3.2. Model catalyst properties

To demonstrate the versatility of the preparation method described above, we have prepared model catalyst covered with nanoparticles with two different compositions; pure Fe and Fe with 10 mol% Mn (Fe and Fe_9Mn_1 respectively). The model cata-
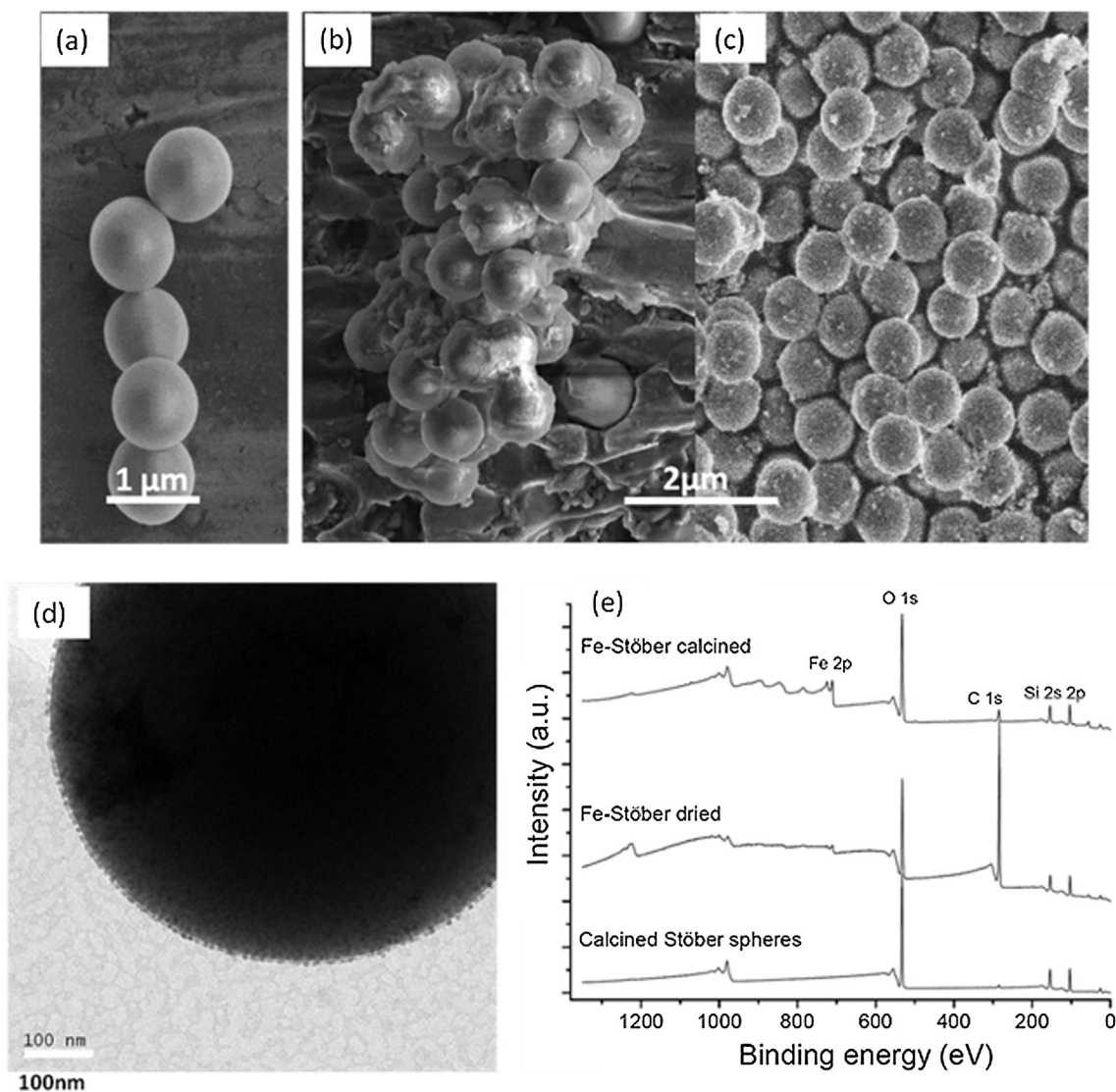

Fig. 1. SEM image (a) calcined SiO_2, (b) dried Fe/SiO_2, (c) calcined Fe/SiO_2, (d) TEM image of calcined Fe/SiO_2, and (e) XPS spectra of the calcined SiO_2, and the dried Fe/SiO_2, and calcined Fe/SiO_2.

Table 1

Properties of the Fe and Fe$_9$Mn$_1$ model catalysts, before and after catalytic testing. Elemental composition estimated from XPS and particle diameters estimated from XRD and TEM.

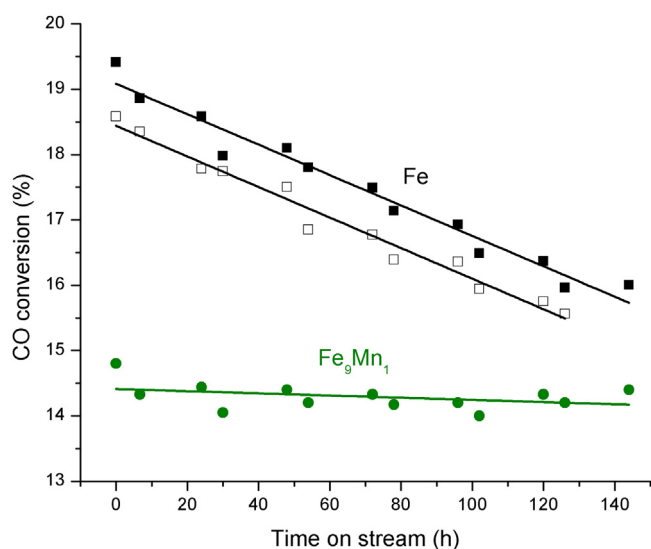| Treatment		After calcination		After FTS	
Sample name		Fe	Fe$_9$Mn$_1$	Fe	Fe$_9$Mn$_1$
Characterization		Elemental Contribution Mol%			
XPS	Element				
	Fe	5.6	5.8	0.5	0.9
	Mn	0	0.9	0	0.2
	Si	27.3	23.8	6.2	6.3
	O	58.3	54.6	6.7	9.8
	C	8.7	11.8	84.5	79.5
	(Fe + Mn)/Si	0.21	0.28	0.08	0.17
TEM		Average particle diameter (nm)			
		8.5	7.5	9.8	8.9
XRD		8.8	7.9	10.2	9.3

Fig. 2. CO conversion and stability of the two Fe/SiO$_2$ (■) & (□) and one Fe$_9$Mn$_1$/SiO$_2$ (●) catalysts. Reaction conditions 270 °C, 13 bar, H$_2$/CO = 1, GHSV = 2300 h^{-1}.

lysts were characterized with XPS, XRD and TEM and the results are summarized in Table 1 (also containing the characterization after catalytic testing). Both elemental composition at the surface and particle sizes are according to expectations, confirming that the metal nanoparticles are not altered by the deposition procedure and that reasonable estimates of the sizes can be achieved both with TEM and XRD.

3.3. FTS synthesis, activity and stability

The following results section describes the catalytic testing of the prepared model catalysts under realistic FTS conditions. Fig. 2 shows the CO conversion and stabilities of two Fe and one Fe$_9$Mn$_1$ catalysts during steady-state runs, after CO pretreatments as described in the experimental section. Both iron catalysts deactivate slowly during the experiment while the CO conversion remains stable for the Mn-promoted sample.

3.4. FTS synthesis, selectivity

The effect of the manganese promoter on the selectivity toward olefins, methane and CO$_2$ are shown in Fig. 3 (note that the selec-
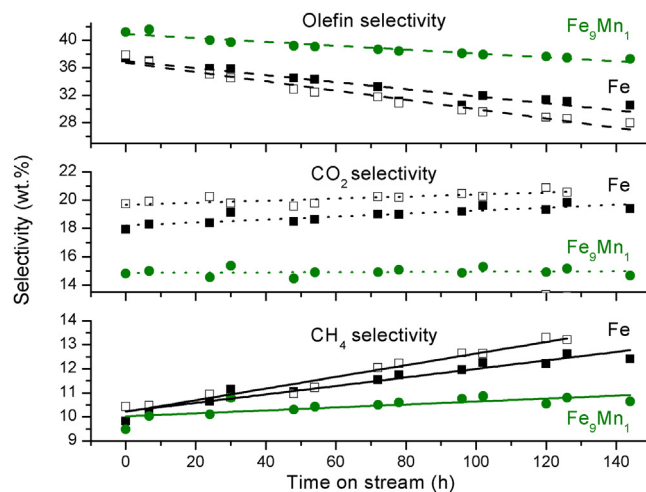

Fig. 3. Selectivities towards olefins (dashed lines), CO$_2$ (dotted lines) and CH$_4$ (solid lines) for the two Fe/SiO$_2$ (■) & (□) and the Fe$_9$Mn$_1$/SiO$_2$ (●). Reaction conditions 270 °C, 13 bar, H$_2$/CO = 1, GHSV = 2300 h^{-1}. Calculated as described in the experimental section.

Table 2

Effect of manganese on the FTS activity and hydrocarbon selectivity by end of the reaction.

Catalyst	Fe	Fe$_9$Mn$_1$
CO conversion (%)	15.9	14.5
Hydrocarbon product distribution (mass%)		
CH$_4$	9.4	8.2
C$_2$	7.8	8
C$_3$	18.6	19
C$_4$	17.9	17.6
C$_5$	16.6	15.9
C$_6$	14	14.2
C$_7$	9	10.7
C$_8$	5.1	6
C$_2$—C$_8$	89	91.4
α (C$_3$—C$_8$)	0.69	0.70

Reaction conditions: *270 °C, 13 bar, H$_2$/CO = 1, 2300 h^{-1}, and 145 h.*

tivities refer to different bases for the hydrocarbons and the CO$_2$ as described in the experimental section).

It is found that the addition of manganese in the catalyst increases the selectivity towards olefin over paraffin (for hydrocarbons of all lengths) and suppresses the formation of CH$_4$ and CO$_2$. Furthermore, the selectivity towards olefins decreases in favor of CH$_4$, for all catalysts during the extent of the experiment.

The detailed FTS activity, selectivity and hydrocarbon distribution of the catalysts at the end of the reaction are summarized in Table 2.

Although the Mn-promoted catalyst produces less CH$_4$ and slightly more of the longer carbon chains, the very similar α value (0.69) for iron and iron-manganese catalysts indicates that manganese has hardly no effect on chain growth according to the Anderson-Schulz-Flory (ASF) distribution.

3.5. Catalyst characterization

The main reasons for using model catalysts in the catalytic tests are that they are well defined and that they can be carefully characterized with a range of techniques. Such characterizations are presented in the following section, aiming at correlating the differences in catalyst activity, stability and selectivity with differences in its fundamental physical properties.
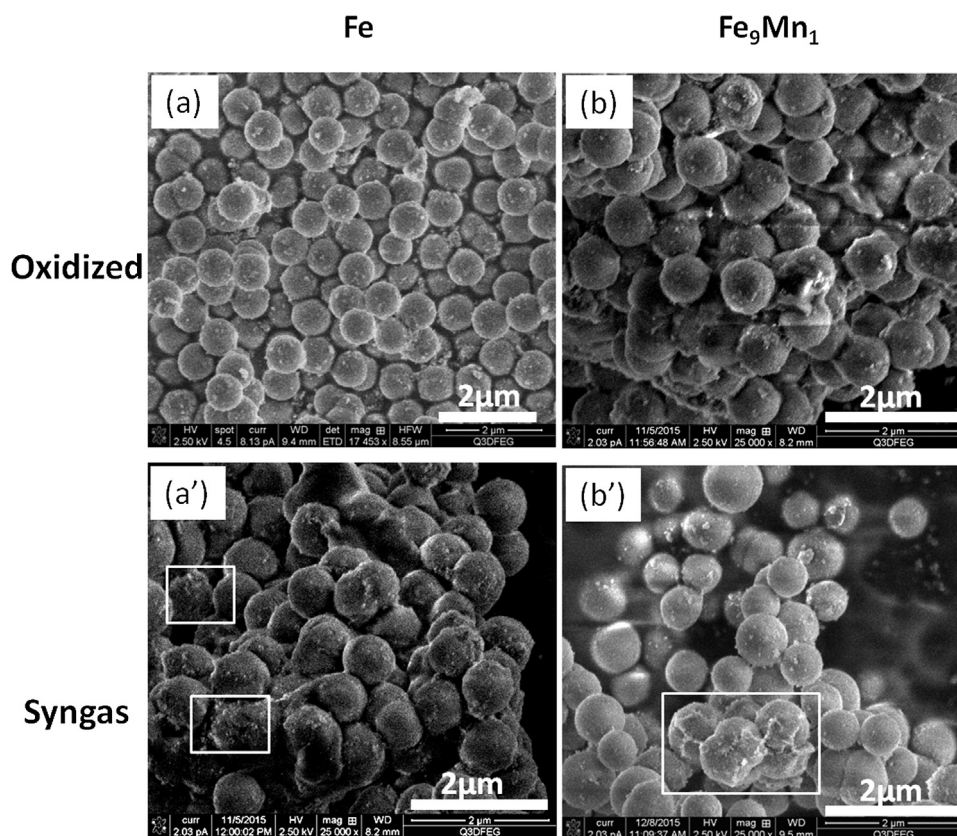
Fe Fe$_9$Mn$_1$

Fig. 4. SEM micrographs of calcined (a) pure Fe/SiO$_2$ and (b) Fe$_9$Mn$_1$/SiO$_2$ and (a') pure Fe/SiO$_2$ and (b') Fe$_9$Mn$_1$/SiO$_2$ after exposure to synthesis gas at 270 °C and 13 bar.

3.5.1. Scanning electron microscopy

SEM images of the model catalysts (Fe and Fe$_9$Mn$_1$) after calcination and after the catalytic testing described above are shown in Fig. 4.

In both cases the presence of metal nanoparticles on the Stöber spheres are obvious from the bright edges. Although SEM is not capturing catalyst properties on the most relevant length scales (nm and below) it gives an indication that no major material deformation or merging/agglomeration of the support occurs. Some minor differences are seen before after catalytic testing as highlighted by the white squares. This could be either due to agglomeration of metal nanoparticles or wax-formation.

3.5.2. Transmission electron microscopy

Fig. 5 shows TEM images of the catalysts with three different magnifications, before and after catalytic testing.

In all cases a large part of the support's surface is covered by the nanoparticles. Comparing the metal nanoparticles after calcination and after syngas treatment under real conditions, a core-shell structure is clearly observed for syngas treated nanoparticles (marked with white squares). These may consist of iron carbide, surrounded by iron and iron-manganese oxides or they may be due to the formation of hydrocarbons/waxes.

As presented in Table 2, most of the metal nanoparticles experienced a small increase in diameter (~1.5 nm) after the catalytic testing, remaining smaller than 10 nm. However, a few particles were found on all spheres (see figures in the right column) with a significantly larger diameter (up to ~30 nm). This can hardly be only because of carbide formation. These are either due to sintering via an Ostwald ripening process or agglomeration of many particles followed by the formation of a core shell structure, or more

likely, encapsulation of the metal nanoparticles in wax or deposited carbon.

3.5.3. X-ray photoelectron spectroscopy

Fig. 6 shows the XPS spectra in the Fe 2p, Mn 2p and C1s regions for the calcined Fe and Fe$_9$Mn$_1$ catalysts, before and after syngas treatment.

For calcined samples the Fe 2p$_{3/2}$ peak (Fig. 6a) is located at 710.7 eV [9,12] and exhibits a satellite peak at 719 eV, characteristic for Fe^{3+} species. The Mn 2p spectra of the Mn-promoted sample (Fig. 6b) exhibit two peaks at 641.6 and 653.4 eV, which can be attributed to the Mn 2p$_{3/2}$ and Mn 2p$_{1/2}$ with binding energies corresponding to MnO$_2$ [13]. The corresponding carbon spectra (Fig. 6c) show a small peak at 284.6 eV due to a small amount of remaining carbon from the sample preparation process and/or adventitious carbon from the sample transfer to the XPS. After the syngas treatment, the Fe 2p$_{3/2}$ peak for Fe and Fe$_9$Mn$_1$ are located at around 710.8 eV while the satellite peak at 719 eV is no longer observed. This indicates that at the surface of the nanoparticles, magnetite (Fe$_3$O$_4$) is the dominant phase. In addition, and more surprisingly, no peak corresponding to metallic iron/iron carbide at around 707 eV is observed. Although the samples are transferred through air, which is known to cause re-oxidation of Fe, some reduced material is usually maintained under the protective oxide surface. The fact that we do not observe any reduced Fe can be either due to oxidizing/reoxidizing of some of the metal particles during the catalytic test or because of insufficient reduction during the activation step. Unreduced particles would be inactive as catalyst while the properly reduced particles are active and thus immersed in wax and not seen in XPS. For the syngas treated Fe$_9$Mn$_1$ sample, a satellite peak appears at 647.5 eV and the Mn 2p$_{3/2}$ is shifted to 641.5 eV, which is significant for MnO. The corresponding carbon
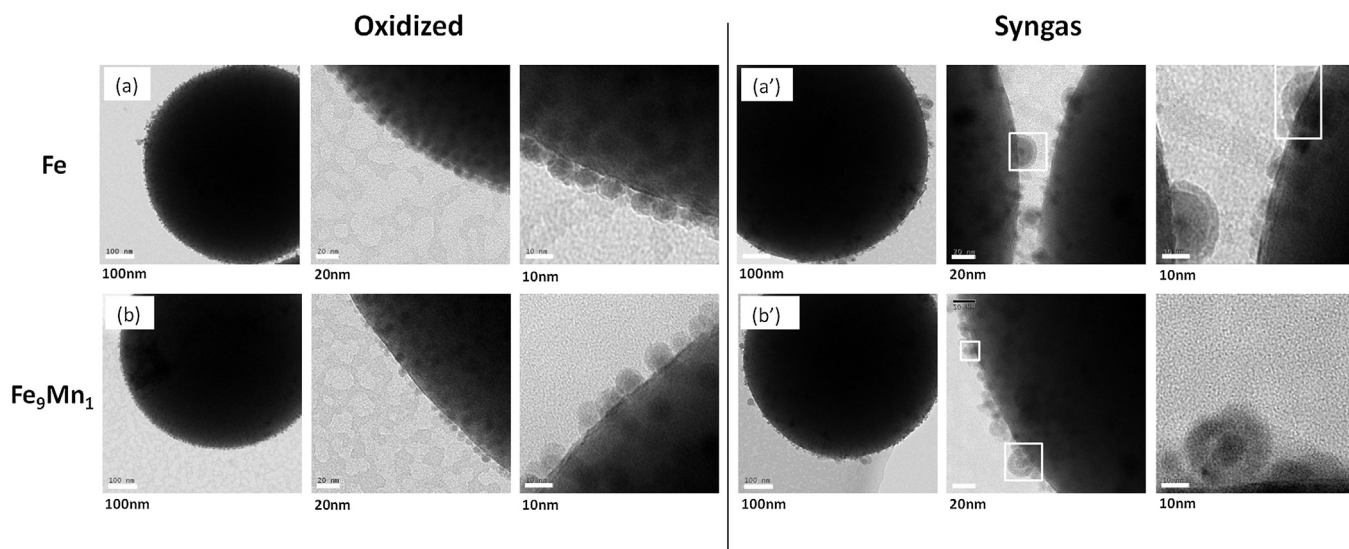
Oxidized

Syngas

Fig. 5. TEM micrographs of calcined (a) pure Fe/SiO$_2$ and (b) Fe$_9$Mn$_1$/SiO$_2$ and (a') pure Fe/SiO$_2$ and (b') Fe$_9$Mn$_1$/SiO$_2$ after exposure to synthesis gas at 270 °C and 13 bar.
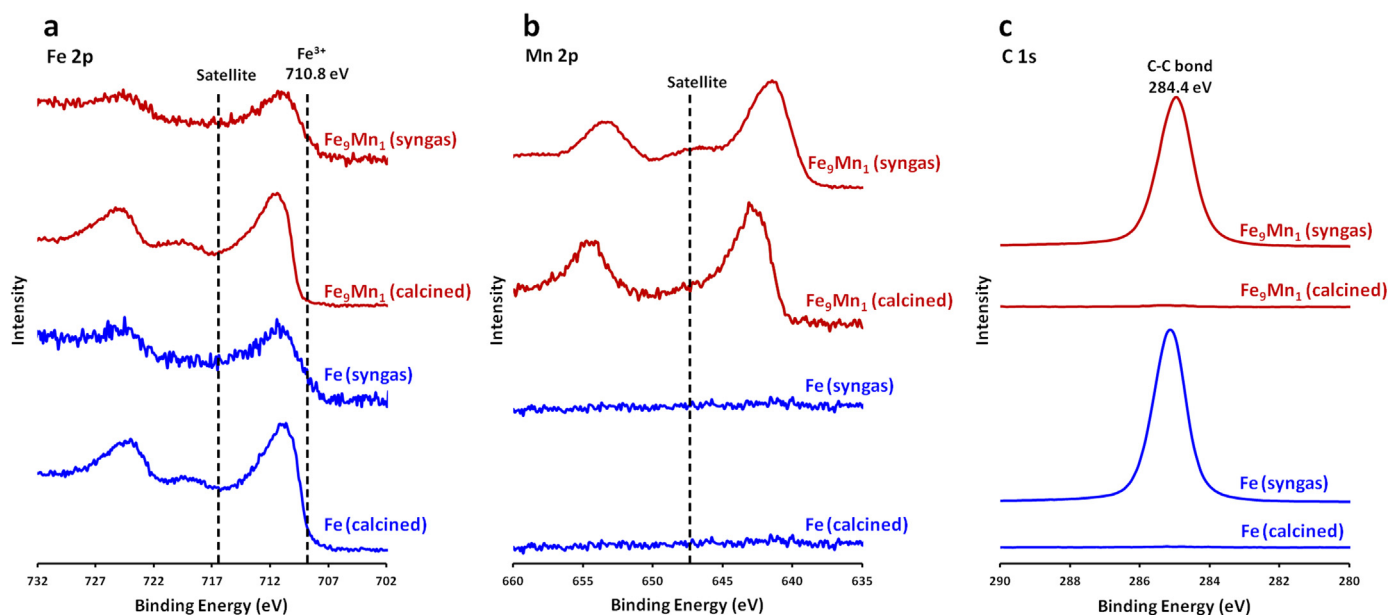

Fig. 6. (a) Fe2p spectra; (b) Mn2p spectra; and (c) C1 s spectra of calcined and syngas treated pure Fe and Fe$_9$Mn$_1$/SiO$_2$ after exposure to synthesis gas at 270 °C and 13 bar. The dash vertical lines shows Fe^{3+} in γ-Fe$_2$O$_3$ (710.8 eV), the Fe^{3+}-satellite (719 eV), the Mn^{2+}(647.5 eV) and graphitic C (∼ 284.5) eV.

spectra (Fig. 6c) show a sharp peak at 284–285 eV due to formation of large amounts of wax (hydrocarbons) at the surface of the catalysts.

The elemental composition of the surface is presented in Table 1. After syngas treatment, the dominating element is carbon from the produced wax. Therefore, the signals from the catalyst itself are very weak and thus hard to interpret. Nevertheless, it appears that the metal/SiO$_2$ ratio is significantly lower after the syngas treatment. This could be either due to sintering or because of preferential adsorption of carbon on the metal nanoparticles leaving the SiO$_2$ support less covered.

3.5.4. X-ray diffraction

Fig. 7 shows the X-ray diffraction of the Fe and Fe$_9$Mn$_1$ catalysts after calcination and syngas treatment taken to identify changes in the crystalline phases.

The intense, broad feature around 2θ = 24° in the overview scans in Fig. 7 (a) correspond to the amorphous SiO$_2$ support (PDF #29-0085). The other diffraction peaks are well fitted with the maghemite (γ-Fe$_2$O$_3$) reference pattern (COD #906316) (the crystal plane indexes (220), (311), (400), (511), and (440) are indicated in the figure). Although the diffraction pattern of the magnetite (Fe$_3$O$_4$) (COD #1011032) does not differ much from maghemite [14], the XPS Fe 2p spectrum (Fig. 6) shows a distinct satellite peak at 719 eV, which is characteristic for Fe^{3+}. Therefore, it can be concluded that the iron nanoparticles at the surface of the calcined spheres are present as maghemite (γ-Fe$_2$O$_3$). The XRD pattern obtained from the Fe$_9$Mn$_1$ sample shows a similar pattern as observed for pure iron and does not contain any additional peaks indicating formation of Mn-ferrite as a separate phase (COD #1010371). This result can be explained either by the fact that the reflections corresponding to the iron-manganese structure is very similar to maghemite (γ-Fe$_2$O$_3$) and therefore not resolved, or due
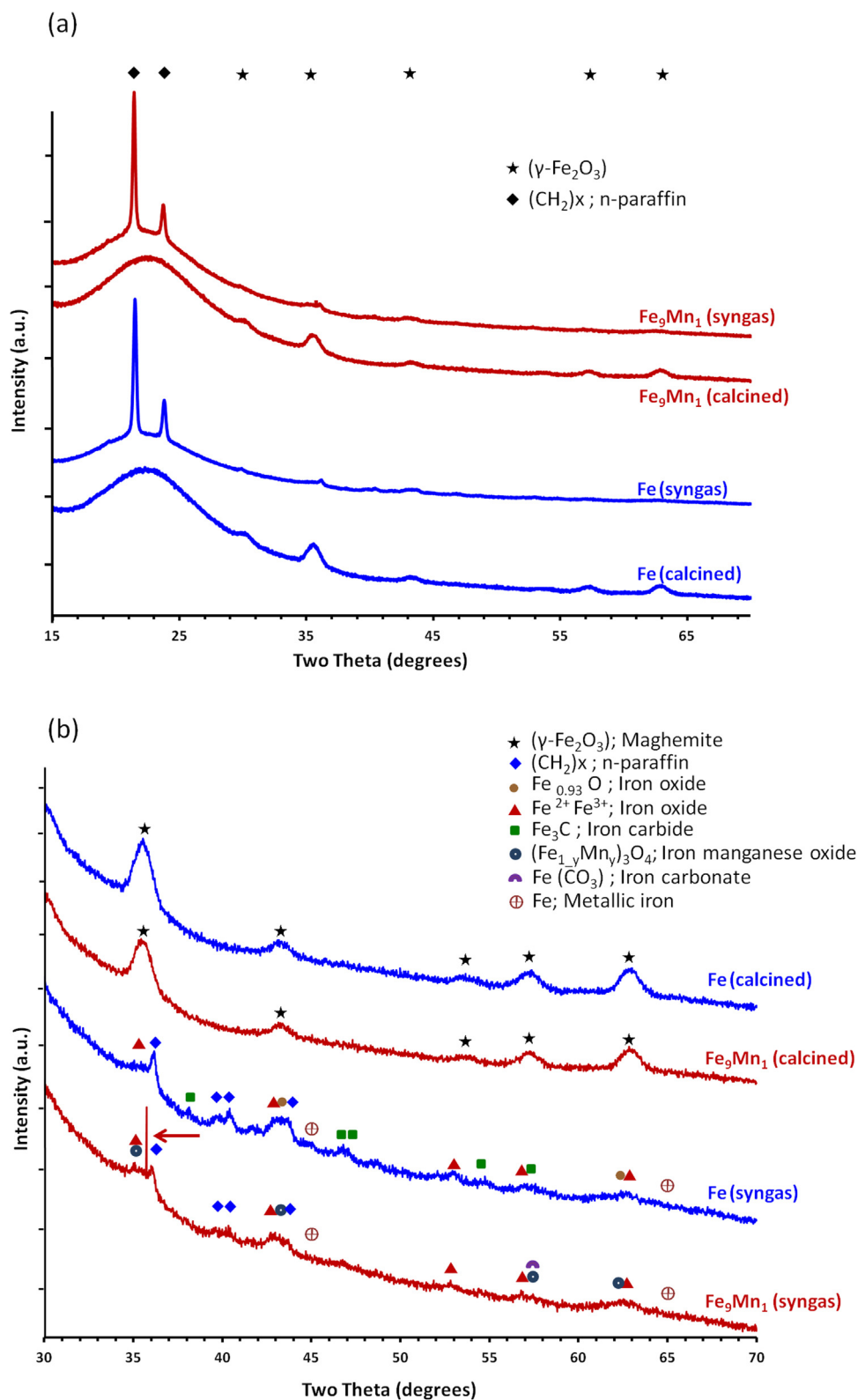
Fig. 7. (a) XRD pattern of the calcined and syngas treated pure Fe & Fe$_9$Mn$_1$ samples and (b) zoom in on the same patterns outside the region dominated by the wax related peaks.

to the formation of an amorphous manganese-phase for the mixed samples. It should also be kept in mind that the Mn constitutes only 10% of the metal content, thus limiting the formation of Mn-ferrite to a maximum of 20% of the total metal related signal making it difficult to detect. The main crystalline phase present in both of the spent catalysts is wax (paraffin) $2\theta = 21.2°$ and $2\theta = 23.8°$ overlapping with the broad amorphous reflection of the silica Stöber supports with additional minor reflections that could possibly be assigned to iron carbides, iron oxides and manganese oxides.

Fig. 7(b) shows the higher magnification X-ray diffraction patterns in the angular range $2\theta = 30$–$70°$, i.e. outside the region dominated by the paraffin related reflections. For the calcined Fe & Fe_9Mn_1-catalysts, the diffraction patterns are very similar, well fitted by the maghemite (γ-Fe_2O_3) reference. After the syngas treatment, the peaks corresponding to γ-Fe_2O_3 are clearly weaker indicating that the catalysts have been reduced. For the Fe sample, the presence of iron oxides and carbides (Fe_3C) can be seen while this is much less pronounced on the Fe_9Mn_1 sample. Suppression of FeC_x formation by Mn-promoters has been reported previously [15]. However, the signals are weak, partly due to low loading of metal, but also because the wavelength of the radiation from the Cu target, which was used for the XRD measurements, causes florescence that result in poor signal to noise ration and attenuation of reflections. To reduce this effect, incident and diffracted beam monochromators, in combination with another X-ray target, such as iron or cobalt could be used, or if only copper radiation is available, much longer data acquisition times are required. The red arrow indicates a spike in the data, which is likely due to an anomaly in the measurement.

3.5.5. ATR-IR

To confirm the presence of hydrocarbons on both the Fe and the Fe_9Mn_1 samples, ATR-IR measurements were carried out. The two upper curves in Fig. 8 show the spectra of the syngas treated samples, marking out the peak positions of all relevant IR peaks. Both spectra show a similar trend: absorptions peaks at $\sim1450\,cm^{-1}$ (ν (C—H)), $\sim1650\,cm^{-1}$ (ν (C=C)), ~2050 and $\sim2200\,cm^{-1}$ (ν (C=C) or C(triple bond) or (=C—H)), as well as two intense peaks at $\sim2870\,cm^{-1}$, $2930\,cm^{-1}$ and a smaller peak at $\sim2950\,cm^{-1}$ attributed to vibration regions of the alkyl (CH_3/CH_2) groups [16]. This confirms the presence of wax and agrees with the results obtained with XRD. The broad peak at $\sim3050\,cm^{-1}$ and $3550\,cm^{-1}$ belongs to the O—H stretching mode of water. This is likely the

water formed during syngas treatment/water gas shift reaction, trapped in the wax. Thermal treatment in argon at $400\,°C$ was applied, which removes the hydrocarbons/waxes as well as O—H groups from the catalysts. This is clearly seen in the corresponding two lower curves in Fig. 8, thus further confirming that the adsorbed carbon species on the used catalysts derive from volatile hydrocarbon species.

4. Discussion

The main goal with the research presented in this paper was to fabricate a 3D model catalyst that fulfills the requirements that exhaustive characterization of the supported metal nanoparticles can be achieved while still allowing catalytic testing under realistic conditions. These criteria are met by the developed model catalysts consisting of monodisperse Fe and FeMn nanoparticles supported on non-porous silica micro spheres. While some of the characterization techniques are easier to use and delivers more precise results on a flat model catalyst, catalytic testing under realistic FTS conditions are not easily achieved on such samples and are to our knowledge missing in the literature. Our measurements show that our model catalysts can be used to perform catalytic testing of both fast and slow reactions and that the catalysts can be characterized with SEM, TEM, XPS, XRD and ATR-IR, while still retaining the high definition of a flat model catalyst. Furthermore, the fact that the catalytically active particles are pre-formed, separately, has the advantage that the exact same particles can be deposited both on flat surfaces and on the 3D-supports, thus assuring that comparison of results from the two systems are useful. For example, the distribution of Fe and Mn within single nanoparticles can be carefully investigated on a conventional TEM window, as described in our previous publication [9], where we could also show that the Fe/Mn ratio of the fabricated metal nanoparticles is in good agreement with the target values. Here, this was also confirmed by induc-
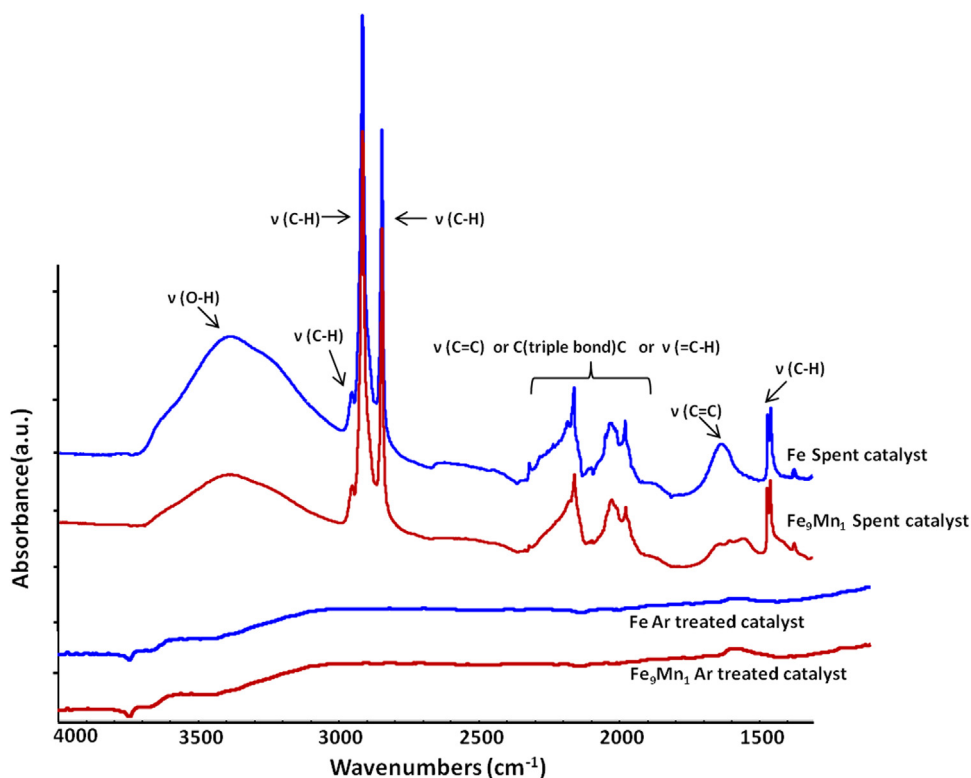

Fig. 8. IR spectra of spent Fe and Fe_9Mn_1/SiO_2 sample (two top spectra) and Ar treated catalysts (two bottom spectra).

tively coupled plasma (ICP) measurements, which showed that the Fe/Mn ratio was 9.8 ± 1, both before and after the catalytic tests. It can then safely be assumed that the particles supported on the 3D silica spheres have the exact same distribution of materials.

In the CO/H_2 oxidation experiments (see supporting information), it was possible to observe transient reduction/oxidation of the catalyst, in real time, from the mass spectrometer signal, a task that is much more difficult on a flat model catalyst. Even more interestingly, the catalytic tests under high pressure FTS conditions, comparing catalysts with and without Mn-promoter shows some clear results. The Fe_9Mn_1 catalyst is less active than the Fe catalyst but simultaneously more stable. Similar observations have been reported in the literature and have then been attributed to that Mn helps stabilizing the active iron carbide phase or that it acts as an electron donor, thereby changing the properties of Fe in a similar manner as alkali promoters [15,17–21]. Mn has also been reported to preserve the dispersion of Fe nanoparticles [9,20,22,23]. Smaller particles have been shown to exhibit less poisoning by carbon deposition, better FeC_x formation properties and thus better CO-hydrogenation behavior.

The other main observation is that the FeMn catalyst exhibits a higher olefin/paraffin ratio in the product stream and suppressed CH_4 and CO_2 production compared to the pure Fe. Although our study does not provide any spectroscopic evidence that can explain these differences, these observations too are in line with literature reports [15,20,22–31]. In these studies, the addition of a Mn promoter is suggested to give rise to electronic effects, promoting dissociative adsorption of CO and suppressing H_2 chemisorption, which increases the selectivity towards olefins. Also, the changed selectivity may be caused by Mn, indirectly, without the need to invoke electronic arguments. For example, if MnO, dispersed throughout the catalyst causes the iron phase to be present in smaller domains, with altered (e.g. rougher or stepped) surface properties, this will also affect the catalytic properties.

Both catalysts were activated following the same standard reduction in CO [32]. Although it has been shown that the presence of Mn in a Fe catalyst can impede its reduction [9,33], there is nothing suggesting that the FeMn catalyst suffers a less complete activation. Rather the opposite, considering its' greater stability during the presented experiments.

5. Conclusion

Preparation of a three-dimensional Fe and mixed FeMn model catalysts has been demonstrated. Pre-formed monodisperse colloidal nanoparticles were deposited on a non-porous support consisting of SiO_2 microspheres (875 ± 25 nm diameter) by a simple mixing and drying procedure. These SiO_2-supported metal nanoparticles form a well-defined model system with properties in between the simplified flat model catalyst and the more complex supported powder catalyst used commercially. We demonstrate that they allow for measurements of catalytic activity in microreactors, where diffusion problems are kept at a minimum while both surface science as well as bulk characterization techniques can be applied.

CO and H_2-oxidation (see supplementary document) as well as FTS activity could be measured. In the FTS reaction, the initial activity decreased with an increase in manganese content. However, CO conversion remained stable for the iron catalysts promoted with manganese. In addition, the Mn-promoter restrained the formation of CO_2 and CH_4 and increased the olefin selectivity, probably because of the strong interaction and interdispersion of iron atoms/ions with manganese oxide. The model catalysts were characterized with electron microscopy (TEM & SEM), XPS, XRD and ATR-IR before and after the catalytic activity tests. All techniques indicated the formation of significant amounts of hydrocarbons (waxes) after the FTS reaction. Surface analysis by XPS reveals that the surface is covered by carbon while the signals coming from the catalytically active materials are weak and hard to interpret. However, there are no signs of metallic or carbidic Fe suggesting re-oxidation/incomplete reduction of the metal nanoparticles surface during or after the catalytic test (syngas treatment). Furthermore, a decreased metal/SiO_2 ratio suggests that carbon deposits preferentially on the metal nanoparticles and not on the SiO_2 support or that sintering occurs. Both suggestions are corroborated by TEM images showing the presence of larger nanoparticles and the build-up of an encapsulating layer. Both ATR-IR and XRD confirms that the encapsulating layer consists of hydrocarbons. The XRD results also revealed the presence of iron oxides and carbides (Fe_3C) phases for the Fe catalyst after syngas treatment while no Fe_3C was observed for the mixed iron-manganese catalysts. In both cases, reduction of the original γ-Fe_2O_3 was observed.

Appendix A. Supplementary data

Supplementary data associated with this article can be found, in the online version, at http://dx.doi.org/10.1016/j.apcata.2017.02.023.

References

[1] P.L.J. Gunter, J.W. Niemantsverdriet, F.H. Riberio, G.A. Somorjai, Cat. Rev. 39 (1997) 77–168.
[2] A.K. Datye, N. Long, Ultramicroscopy 25 (1988) 203–208.
[3] A.K. Datye, Top. Catal. 13 (2000) 131–138.
[4] J. van de Loosdrecht, F.G. Botes, I.M. Ciobica, A. Ferreira, P. Gibson, D.J. Moodley, A.M. Saib, J.L. Visagie, C.J. Weststrate, J.W. Niemantsverdriet, Fischer-Tropsch synthesis: catalysts and chemistry, in: J. Reedijk, K. Poeppelmeier (Eds.), Comprehensive Inorganic Chemistry II, Second Ed.,: from Elements to Applications, Elsevier, Amsterdam, 2013.
[5] J. van de Loosdrecht, I.M. Ciobîca, P. Gibson, N.S. Govender, D.J. Moodley, A.M. Saib, C.J. Weststrate, J.W. Niemantsverdriet, ACS Catal. 6 (2016) 3840–3855.
[6] W. Stöber, A. Fink, E. Bohn, J. Colloid Interface Sci. 26 (1968) 62–69.
[7] J. Park, K. An, Y. Hwang, J.G. Park, H.J. Noh, J.Y. Kim, J.H. Park, H.M. Hwan, T. Hyeon, Nat. Mater. 3 (2004) 891–895.
[8] T.D. Schladt, T. Graf, W. Tremel, Chem. Mater. 21 (2009) 3183–3190.
[9] M. Dad, H.O.A. Fredriksson, J. van de Loosdrecht, P.C. Thüne, J.W. Niemantsverdriet, Catal. Struct. React. 1 (2015) 101–109.
[10] Rasband, W.S., Image J, U. S. National Institutes of Health, Bethesda, Maryland, USA, http://imagej.nih.gov/ij/, 1997–2012.
[11] N.S. Govender, M.J. van Vuuren, M. Claeys, E. Van Steen, Ind. Eng. Chem. Res. 45 (2006) 8629–8633.
[12] T. Yamashita, P. Hayes, Appl. Surf. Sci. 254 (2008) 2441–2449.
[13] M.C. Biesinger, B.P. Payne, A.P. Grosvenor, L.W.M. Lau, A.R. Gerson, R.St.C. Smart, Appl. Surf. Sci. 257 (2011) 2717–2730.
[14] K. Woo, J. Hong, S. Choi, H.-W. Lee, J.-P. Ahn, C.S. Kim, S.W. Lee, Chem. Mater. 16 (2004) 2814–2818.
[15] A. Campos, N. Lohitharn, A. Roy, E. Lotero, J.G. Goodwin Jr, J. Spivey, Appl. Catal. A Gen. 375 (2010) 12–16.
[16] I.R. Hill, I.W. Levin, J. Chem. Phys. 70 (1979) 2.
[17] T. Herranz, S. Rojas, F.J. Perez-Alonso, M. Ojeda, P. Terreros, J.L.G. Fierro, Appl. Catal. A. 311 (2006) 66–75.
[18] J. Xu, C.H. Bartholomew, J. Phys. Chem. B. 109 (2005) 2392–2403.
[19] J.A. Amelse, J.B. Butt, L.H. Schwartz, J. Phys. Chem. 82 (1978) 558–563.
[20] K.B. Jensen, F.E. Massoth, J. Catal. 92 (1985) 109–118.
[21] T. Herranz, S. Rojas, F.J. Perez-Alonso, M. Ojeda, P. Terreros, J.L.G. Fierro, J. Catal. 243 (2006) 199–211.
[22] J. Barrault, C. Renard, Appl. Catal. 14 (1985) 133–143.
[23] J.J. Venter, A. Chen, M.A. Vannice, J. Catal. 117 (1989) 170–187.
[24] G.C. Maiti, R. Malessa, M. Baerns, Appl. Catal. 5 (1983) 151–170.

[25] Z. Tao, Y. Yang, C. Zhang, T. Li, M. Ding, H. Xiang, Y. Li, J. Nat. Gas Chem. 16 (2007) 278–285.
[26] N. Lohitharn, J.G. Goodwin, J. Catal. 257 (2008) 142–151.
[27] Y. Zhang, L. Ma, J. Tu, T. Wang, X. Li, Appl. Catal. A Gen. 499 (2015) 139–145.
[28] W.L. van Dijk, J.W. Niemantsverdriet, A.M. van de Kraan, H.S. van der Baan, Appl. Catal. 2 (1982) 273–288.
[29] L.Y. Xu, Q.X. Wang, Y.D. Xu, J.S. Huang, Catal. Lett. 31 (3) (1995) 253.
[30] C.K. Das, N.S. Das, D.P. Choudhury, G. Ravichandran, D.K. Chakrabarty, Appl. Catal. A. 111 (1994) 119–132.
[31] Y. Liu, B.T. Teng, X.H. Guo, Y. Li, J. Chang, L. Tian, X. Hao, Y. Wang, H.W. Xiang, Y.Y. Xu, Y.W. Li, J. Mol. Catal. A. Chem. 272 (2007) 182–190.
[32] R.J. O'Brien, L. Xu, R.L. Spicer, B.H. Davis, Energy Fuels. 10 (1996) 921–926.
[33] T. Grzybek, H. Papp, M. Baerns, Appl. Catal. 29 (1987) 335–350.